ACS NANO
Cite This: ACS Nano 2018, 12, 11600−11609
www.acsnano.org

ARTICLE

Tumor-Vasculature-on-a-Chip for Investigating Nanoparticle Extravasation and Tumor Accumulation

Hao-Fei Wang,[†] Rui Ran,[†] Yun Liu,[†] Yue Hui,[†] Bijun Zeng,[‡] Dong Chen,[§,∥] David A. Weitz,[⊥] and Chun-Xia Zhao*[,†]

[†]Australian Institute for Bioengineering and Nanotechnology, The University of Queensland, St Lucia, QLD 4072, Australia
[‡]Diamantina Institute, The University of Queensland, St Lucia, QLD 4072, Australia
[§]State Key Laboratory of Fluid Power and Mechatronic Systems, Zhejiang University, Zheda Road, No. 38, Hangzhou, 310027, People's Republic of China
[∥]Institute of Process Equipment, College of Energy Engineering, Zhejiang University, Zheda Road, No. 38, Hangzhou, 310027, People's Republic of China
[⊥]John A. Paulson School of Engineering and Applied Sciences and Department of Physics, Harvard University, Cambridge, Massachusetts 02138, United States

Supporting Information

ABSTRACT: **Nanoparticle tumor accumulation relies on a key mechanism, the enhanced permeability and retention (EPR) effect, but it remains challenging to decipher the exact impact of the EPR effect. Animal models in combination with imaging modalities are useful, but it is impossible to delineate the roles of multiple biological barriers involved in nanoparticle tumor accumulation. Here we report a microfluidic tumor-vasculature-on-a-chip (TVOC) mimicking two key biological barriers, namely, tumor leaky vasculature and 3D tumor tissue with dense extracellular matrix (ECM), to study nanoparticle extravasation through leaky vasculature and the following accumulation in tumor tissues. Intact 3D tumor vasculature was developed with selective permeability of small molecules (20 kDa) but not large ones (70 kDa). The permeability was further tuned by cytokine stimulation, demonstrating the independent control of the leaky tumor vasculature. Combined with tumor spheroids in dense ECM, our TVOC model is capable of predicting nanoparticles' *in vivo* tumor accumulation, thus providing a powerful platform for nanoparticle evaluation.**

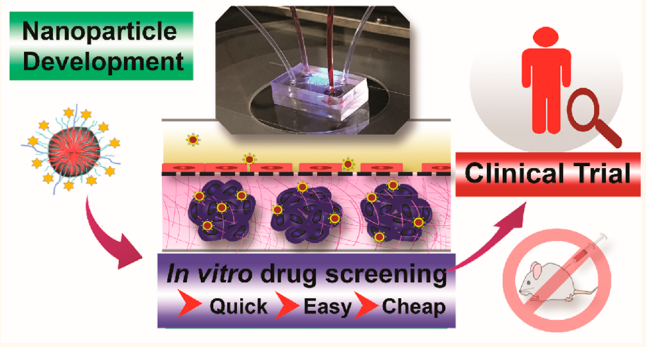

KEYWORDS: *nanoparticles, tumor accumulation, tumor microenvironment, EPR effect, microfluidics*

Nanomaterials have attracted enormous interest in cancer therapeutics during the past two decades because of their potentials in improving the bioavailability of poorly soluble drugs, prolonging circulation time, and reducing drug toxicity.[1,2] With the success of several nanoparticle (NP) platforms, such as liposomes and protein-bound NPs, many more formulations are under clinical trial. However, the efficient accumulation of NPs in tumor tissues remains challenging due to the lack of fundamental understanding of the complex biological barriers involved in the transport of NPs.

Due to the chaotic growth of tumor, tumor tissues generally develop leaky tumor vasculature and defective lymphatic drainage, which promote preferential accumulation and retention of nanoparticles at tumor. The phenomenon is known as the enhanced permeability and retention (EPR) effect, which has become the principle of NPs' design. The vasculature represents one of the most significant barriers to the delivery of NPs, which controls the permeability of vasculature to molecules and nanoparticles, followed by another barrier posed by the dense extracellular matrix consisting of cross-linked networks of collagen and fibers, which hinders tumor penetration of NPs. These key biological barriers play a critical role in the systemic delivery of NPs to

Received: September 6, 2018
Accepted: October 31, 2018
Published: October 31, 2018

DOI: 10.1021/acsnano.8b06846
ACS Nano 2018, 12, 11600−11609

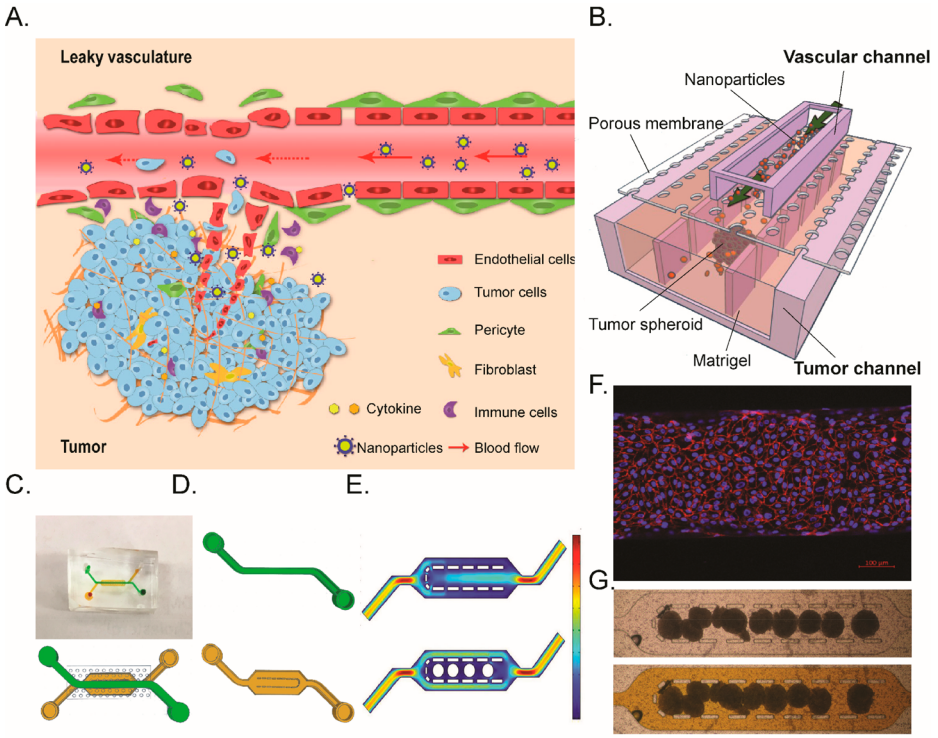

Figure 1. Design of the tumor-vasculature-on a-chip (TVOC). (A) Schematic of the *in vivo* tumor microenvironment consisting of leaky vasculature and tumor tissues. (B) Schematic illustration of the *in vitro* TVOC model. The double-layer device consists of two layers of microchannels with a porous membrane sandwiched between these two layers. The top channel is for developing 3D tumor vasculature, while the bottom channel is for mimicking tumor tissue by incorporating tumor spheroids and the surrounding gel matrix. (C) Photo of the fabricated double-layer PDMS device with green dye filling the top channel and yellow dye filling the bottom channel. (D) Design of the top and bottom channels of the TVOC. The top channel is straight, allowing steady medium perfusion for culturing endothelial cells, while the bottom channel (yellow) is designed with a central region for trapping tumor spheroids. (E) Computational simulation of the fluid velocity in the bottom channel before and after the loading of spheroids. (F) Confocal image of a confluent HUVEC monolayer formed in the top channel. Cells were stained for VE-cadherin (red) and nucleus (blue). Scale bar represents 100 μm. (G) Microscopy images of spheroids trapped in the bottom channel. After spheroids were loaded, the bottom channel was perfused with a yellow dye from the inlet on the right, and the image shows no change of the tumor spheroids' structure and position.

tumor tissues.[3,4] A fundamental understanding of these barriers will provide clearer rules for designing better NPs for drug delivery. Although a few microfluidic systems have been developed to study NP intratumoral diffusion and tumor cell binding,[5−8] or to mimic tumor vasculature and study vascular permeability of NPs,[9−12] none of them examine the combined effect of the consequential key barriers that affect NP tumor accumulation, including extravasation across endothelial barriers, penetration into a rigid tumor matrix, and internalization in tumor cells. More importantly, fewer microfluidic tumor models have been validated using animal models.

In this study, we report a tumor-vasculature-on-a-chip (TVOC) model that recapitulates the key barriers involved in the EPR effect, including endothelial barriers, dense extracellular matrix (ECM), and 3D tumor tissue, to closely investigate NP extravasation and tumor accumulation. The TVOC model consists of a top vascular channel and a bottom tumor channel separated by a porous membrane, allowing the coculture of human umbilical vein endothelial cells (HUVECs) in the top channel and 3D tumor spheroids composed of human ovarian cancer cells (SKOV3) in the bottom channel. We first established the leaky tumor vasculature and examined its barrier function by conducting a permeability assay using model NPs (20 and 70 kDa dextran, liposomes, and polymer NPs). Then tumor spheroids embedded in an extracellular matrix were incorporated to complete the tumor compartment. The tumor accumulation of NPs with and without a targeting ligand was evaluated using the established TVOC, and the results were further validated using an *in vivo* murine xenograft model.

RESULTS

Design of the Tumor-Vasculature-on-a-Chip. The TVOC model is designed to have a two-layer structure sandwiching a porous polydimethylsiloxane (PDMS) membrane with pore sizes of 10 μm in diameter, aiming to recapitulate the key features of the tumor microenvironment (Figure 1A and B). The top microchannel (green channel in Figure 1C and D) is to develop a tumor vasculature structure by culturing HUVECs. The bottom microchannel (orange channel in Figure 1C and D) is designed with a central expanded region outlined by rectangular pillars for tumor spheroid entrapment. The fabricated TVOC device (Figure 1C) has the size of a small coin. The simulation of the velocity profile across the bottom channel before and after spheroid trapping (Figure 1E) shows that when loading spheroids, the high velocity toward the central trapping region forces spheroids to move along the pillars and enter the trapping region. After the spheroids are trapped, the flow velocity in the central channel is greatly reduced, and the excess inlet fluid is split into two streams and exits via the two side channels, leaving the central region undisturbed. Our experiments show

DOI: 10.1021/acsnano.8b06846
ACS Nano 2018, 12, 11600−11609

that confluent HUVEC monolayers are successfully developed in the top channel of the TVOC (Figure 1F), and the bottom channel is capable of immobilizing multiple tumor spheroids in the central region (Figure 1G), which agrees well with the simulation result.

Formation of 3D Vasculature with a Confluent HUVEC Monolayer. To develop a functional endothelial barrier, we studied the effect of medium perfusion rates on the formation of tight intercellular junctions. HUVECs were cultured under low perfusions for 24 h to enhance cell attachment and then subjected to increased perfusion rates of up to 2.56 μL/min (corresponding to 1 mm/s, 0.3 dyn/cm^2) for another 24 h. Compared to the static condition, medium perfusion induced shear force on HUVECs, promoting organized cell arrangement and formation of intercellular junctions, as indicated by throughout expression of VE-cadherin at cell borders (Figure 2A). Increased perfusion rates

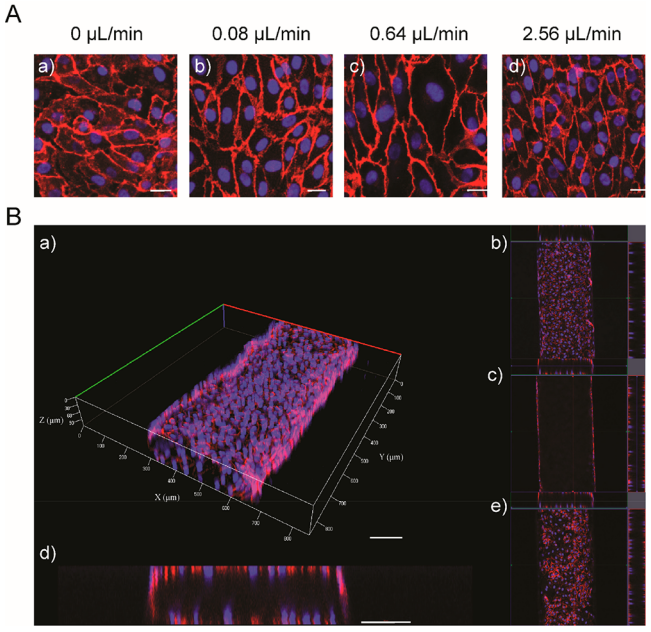

Figure 2. Confocal images of the endothelialized microchannel. (A) Immunostaining shows the effect of flow rate on the expression of adherens junction protein VE-cadherin (red) after 24 h of medium perfusion. Scale bars represent 20 μm. (B) Z-stacking confocal images showing the 3D structure of vasculature (a; scale bars represent 100 μm), with a view of the $X-Y$ plane at the top (b), middle (c), and bottom (e) of the microchannel, and (d) a cross-sectional view of the vasculature. Scale bar is 100 μm. Cells were stained for VE-cadherin (red) and nucleus (blue).

resulted in cell elongation along the direction of shear force (Figure 2A (b,c)), until the elevated shear stress disrupted cell−cell connections (Figure 2A (d)). To ensure the integrity of the HUVEC vasculature with tight intercellular junctions while applying physiologically relevant shear force upon cells, we selected a moderate perfusion rate of 0.64 μL/min for the following HUVECs culture, which gave a linear velocity of 0.3 mm/s, similar to the average blood velocity in capillaries *in vivo*.[13] Figure 2B shows the 3D structure of the endothelilized microchannel with complete HUVEC coverage on all four walls, confirming the formation of 3D vasculature structure with intact intercellular junctions.

Tuning Permeability of the HUVEC Monolayer with TNF-α Stimulation. To mimic the impaired tumor vasculature with elevated vascular permeability, the confluent HUVEC monolayers were treated with tumor necrosis factor-α (TNF-α), a proinflammatory cytokine that induces endothelial barrier dysfunction.[14,15] Confluent HUVEC monolayers were treated with 20 ng/mL TNF-α for up to 2 h under static conditions. F-actin and VE-cadherin were immunostained to examine actin filament organization and intercellular connections. After 1 h of TNF-α stimulation, the VE-cadherin expression at cell borders became weak and discontinuous with a few intercellular gaps appearing. Increasing the stimulation time to 2 h caused significant loss of cell-to-cell contacts with a great increase in the number of intercellular gaps on the cell borders (Figure 3A). The size of intercellular gap openings was analyzed quantitatively (Figure 3B), and 2 h of TNF-α stimulation resulted in a total intercellular gap area of 4.3 ± 0.3%, with an average gap area of 6.6 ± 1.3 μm^2 (2.5 μm in diameter), which was comparable to the sizes of intercellular gaps observed *in vivo* (~2 μm in diameter).[16−18]

At the end of TNF-α stimulation, vascular permeability of untreated and treated HUVEC monolayers was measured by using two model molecules, 20 and 70 kDa dextran. Dextran of 20 kDa could easily pass through the endothelial barrier, while 70 kDa dextran represents large molecules such as albumin (68 kDa), which are relatively impermeable to healthy blood vessels.[19] The permeability coefficients (P) of dextran (Figure 3C) show that the untreated HUVEC monolayers greatly hindered the passage of 70 kDa dextran, suggesting a well-established endothelial barrier with tight intercellular junctions (P = (7.9 ± 1.4) × 10^{-7} cm/s). In contrast, the TNF-α stimulation leads to over a 10-fold increase of the permeability of 70 kDa dextran to (1.0 ± 1.7) × 10^{-5} cm/s. Meanwhile, similar permeability was obtained for 20 kDa dextran ((1.1 ± 1.3) × 10^{-5} cm/s) before and after TNF-α treatment. The selective permeability of vasculature to small molecules (20 kDa dextran) rather than large molecules (70 kDa dextran) demonstrates the size-selective sieving property of the developed intact endothelial barriers. By TNF-α stimulation, intercellular gaps can be tuned and thus a tunable permeability is obtained, allowing the independent study of the correlation between permeability and particle extravasation.

NP Transport in the TVOC through the Endothelial Barrier and Tumor ECM. After the successful establishment of the endothelial barrier with confirmed key characteristics similar to the leaky tumor vasculature *in vivo*, we further explored extravasation and tumor penetration of two different types of NPs, namely, liposomes and poly(ethylene glycol)/poly(lactide-*co*-glycolic acid) nanoparticles (PEG-PLGA NPs). Liposomes and PEG-PLGA NPs are two widely studied systems accounting for more than 80% of nanotechnology-based therapeutic products in clinical applications.[20−22] To ensure valid comparison studies, both NPs were fluorescently labeled for imaging and PEGylated to have a similar surface property, namely, PEG-liposome and PEG-PLGA NPs. Both NPs were synthesized using a facile one-step microfluidic method and had a similar size around 70 nm (Figure S2 in the Supporting Information).[23−26] The permeability assay shows that compared to dextran, slow transmembrane transports were observed for both NPs due to their large particle sizes (Figure 4A), with obtained P values of (9.1 ± 0.2) × 10^{-6} and (7.4 ± 0.3) × 10^{-6} cm/s for PEG-liposomes and PEG-PLGA NPs (Figure 4B), respectively.

DOI: 10.1021/acsnano.8b06846
ACS Nano 2018, 12, 11600−11609

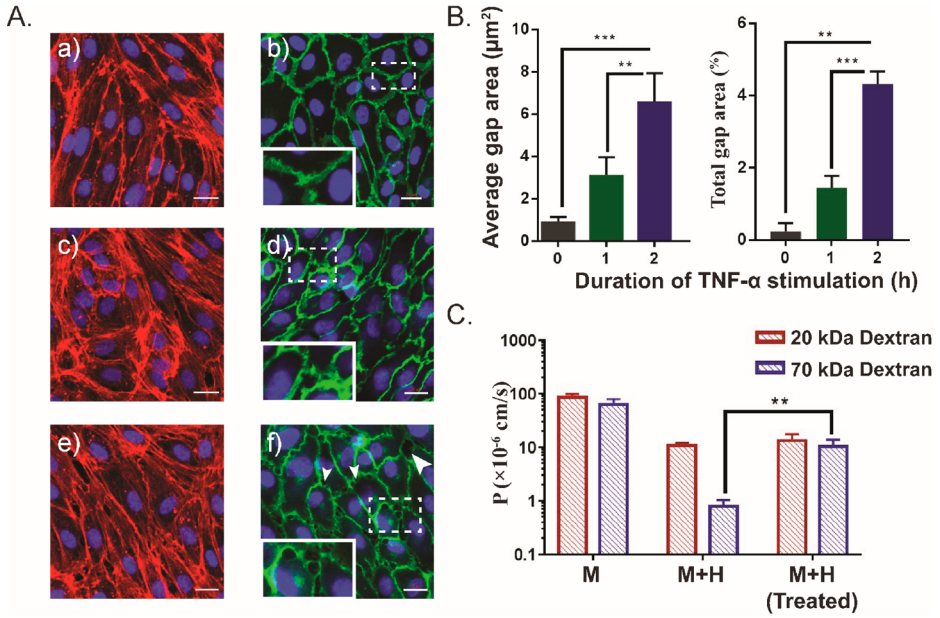

Figure 3. Effect of TNF-α stimulation on confluent HUVEC monolayers in the microchannel. (A) Confocal images of HUVECs without any treatment (a, b) and exposed to 20 ng/mL TNF-α for 1 h (c, d) and 2 h (e, f). Cells were stained for cell nucleus (blue), VE-cadherin (green), and F-actin (red). Intercellular gap openings are indicated by white arrowheads. Scale bars are 20 μm. (B) Quantification of intercellular gap area (n = 6). (C) Calculated permeability coefficients for 20 and 70 kDa dextran across the porous membrane (M) and membrane cultured with confluent HUVEC monolayer (M+H) and with 2 h TNF-α treated HUVEC monolayer (M+H Treated). Data show mean values and SD (n = 3). ** and * represent statistically significant differences $p < 0.01$ and $p < 0.001$, respectively.**

In addition to the endothelial barrier investigated above, the rigid tumor ECM, consisting of a dense collagen network and a high level of space-filling protein and glycosaminoglycans (GAG), poses another barrier to the transport of NPs.[27,28] With this TVOC model, we are able to address key questions about individual barriers as well as the combined effect of multiple barriers. We define the two individual barriers as the endothelial barrier (M+H Treated), the ECM barrier (M+G), and the combined effect of these two barriers (M+G+H Treated). To mimic the collagen-rich tumor ECM, we used Matrigel to provide *in vivo*-like biochemical composition and physical properties of the tumor ECM. The permeability assay showed that similar P values were obtained in the endothelial barrier (M+H Treated) and the dense gel structure (M+G), despite the fact that the transport of NPs across the porous membrane was expected to be faster as the pores on the membrane are much larger than NP size ($P = (9.2 \pm 1.6) \times 10^{-6}$ cm/s for PEG-liposomes and $(8.3 \pm 1.1) \times 10^{-6}$ cm/s for PEG-PLGA NPs). However, in the M+H+G (Treated) model, where both endothelial barrier and dense gel matrix were recreated, the P values of PEG-liposomes and PEG-PLGA NPs dropped significantly to $(1.4 \pm 0.6) \times 10^{-6}$ and $(9 \pm 3.1) \times 10^{-7}$ cm/s, respectively (Figure 4C). The fluorescent intensity profiles of the bottom channel (Figure 4D) reveal the different transportation kinetics of NPs through the engineered tumor vasculature and dense tumor ECM. In the endothelial barrier models (Figure 4D (a)), NPs slowly entered the bottom channel and gradually diffused across the channel. While in the dense gel model (Figure 4D (b)), NP extravasation was rapid, but high accumulation of NPs was observed near the center of the bottom channel. NPs were found to penetrate into Matrigel at a lateral distance of 150 μm within 1 h. When both endothelial barrier and dense ECM were simulated (Figure 4D (c)), the NP extravasation was slow, and further reduced penetration depth of around 30 μm into Matrigel was observed; the low level of migrated NPs resulted in significantly decreased P value of NPs. These results confirm the barrier functions of the developed tumor vasculature and ECM structure. The P values obtained in the TVOC were comparable to results obtained using NPs with similar sizes in *in vitro* models (10^{-6}–10^{-7} cm/s),[10,29] but slightly higher than some results obtained from *in vivo* models (10^{-7}–10^{-8} cm/s).[30−32] This is mainly due to the heterogeneous structure of different tumors or tumor models. Nevertheless, our results demonstrated that the TVOC model is able to recapitulate the key biological barriers involved in the EPR effect and can be applied for further nanoparticle uptake studies.

NP Tumor Accumulation Using the TVOC Model and Animal Models. The complete TVOC model was established by loading SKOV3 tumor spheroids into the bottom channel together with prechilled Matrigel, followed by incubation at 37 °C for polymerization. The confocal images (Figure 5A) show the 3D structure of the TVOC with engineered leaky tumor vasculature in the top channel and tumor spheroids embedded in the bottom channel. To study tumor spheroid uptake in the TVOC, the NPs were introduced into the top channel. After 6 h of perfusion, the spheroids were harvested from the bottom channel for flow cytometry test.

To investigate the NPs' specific and nonspecific interactions with tumors and their cellular uptake, folate receptor targeted liposomes (FA-liposomes) and PEG-PLGA NPs (FA-PLGA NPs) were synthesized with folic acid (FA) as the targeting ligand. FA-liposomes and FA-PLGA NPs produced using the same microfluidic approach[25] had similar sizes of 83.3 ± 2.5 nm in diameter (Figure S3 in the Supporting Information). For comparison, NPs' cellular uptake was also investigated using 2D cell monolayers and 3D tumor spheroids (Figure 5B). From the results, we found that in the 2D cell monolayer model FA-modification enhanced cellular uptake for both liposomes and PLGA NPs compared to untargeted counter-

DOI: 10.1021/acsnano.8b06846
ACS Nano 2018, 12, 11600−11609

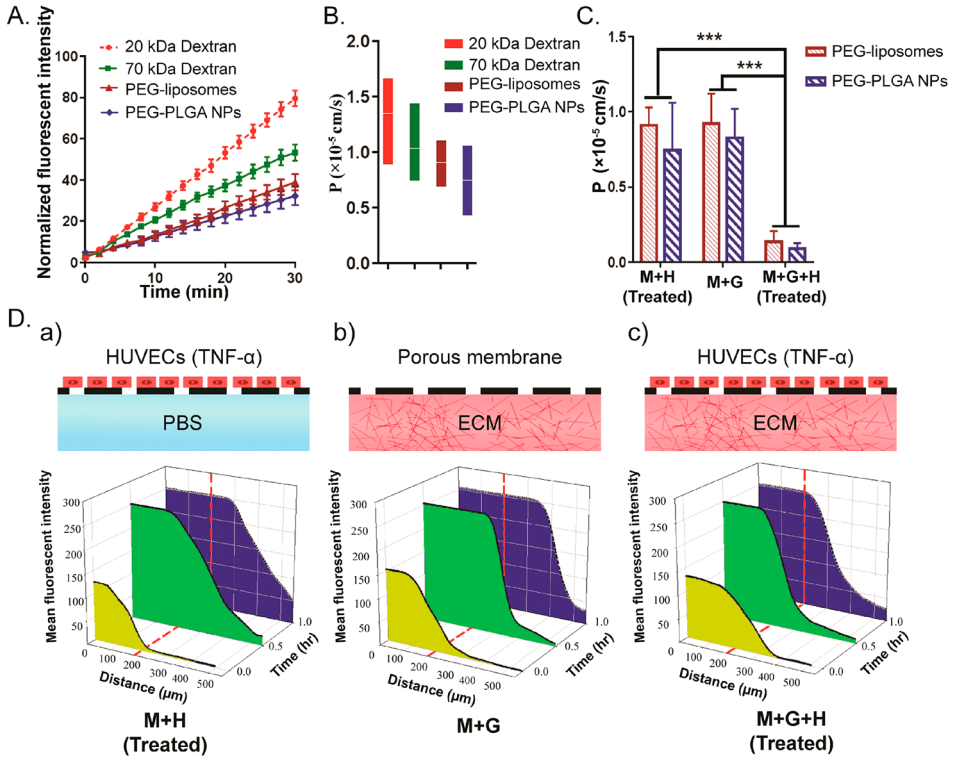

Figure 4. Permeability coefficients of fluorescent NPs (PEG-liposomes and PEG-PLGA NPs) in our TVOC model under different conditions. (A) Changes of mean fluorescent intensity of the bottom channel with time when dextran or NPs were applied to the engineered tumor vasculature. (B) Permeability coefficients of dextran and NPs in the tumor vasculature model. (C) Permeability coefficients of NPs in TVOC. Microfluidic devices were set up with three conditions, the treated HUVEC vasculature at the top and PBS at the bottom (M+H Treated), no cells at the top and Matrigel at the bottom (M+G), treated HUVEC vasculature at the top and Matrigel at the bottom (M+H+G Treated). Mean fluorescence intensity of the bottom channel at each point was extracted from the Zen software (blue edition) for quantitative image analysis. Data show mean values and SD (n = 3). * represents statistically significant difference $p < 0.001$. (D) Corresponding illustration of the microfluidic device setups and time-lapse mean fluorescent intensity profiles against distance to the central of the bottom channel when applying PEG-liposome to TVOC. The edge of the top channel was labeled by vertical red dotted lines at a distance of 200 μm.**

parts. Moreover, the rigid PEG-PLGA NPs exhibited a much higher cellular uptake than the soft PEG-liposomes, which agrees well with findings in the literature that increased rigidity of NPs promotes tumor cellular uptake.[33−35] In comparison, NPs showed much lower overall uptake in 3D spheroids for both the targeted and untargeted liposomes and PLGA NPs, while the targeted formulations still demonstrated their superior cellular uptake to untargeted ones. Similarly, the rigid PLGA NPs exhibit higher tumor spheroid uptake than the liposomes. In contrast, for both liposomes and PLGA NPs, the targeted and untargeted NPs showed no significant cellular uptake differences in the TVOC.

To further evaluate the TVOC model, we established an *in vivo* SKOV3 xenograft tumor model using nude mice. We used PLGA NPs to carry out animal experiments as PLGA NPs showed a higher cellular uptake level. Figure 6A shows the whole animal images of the biodistribution of PEG-PLGA NPs (left) and FA-PLGA NPs (right) at 2 and 6 h after NP injection. At 2 h postinjection, weak fluorescent signals started to appear at the tumor site, while relatively strong fluorescence signals were observed in the spleen and liver. At 6 h postinjection, the fluorescent intensity of both FA-PLGA NPs and PEG-PLGA NPs at the tumor site increased. Quantitative image analysis (Figure 6B) shows that the FA-modification slightly enhanced the accumulation of PLGA NPs in the *in vivo* SKOV3 tumor model compared to the PEG-PLGA NPs, but not significantly (P = 0.56). For comparison, the tumor accumulation of FA-PLGA NPs was normalized against the PEG-PLGA NPs using the fluorescent intensity ratios (Figure 6C). The accumulations of FA-PLGA in both the TVOC and animals were slightly higher than that of the PEG-PLGA, but not statistically significantly.

DISCUSSION

Our TVOC model offers an evaluation model for investigating the key barriers involved in NP extravasation and tumor accumulation, including the leaky vasculature and 3D tumor structure with dense ECM. The design of such a double-layer device enables independent customization of vasculature and tumor compartment to recreate specific physiological conditions by changing shear force, cytokine stimulation, gel density, and cell types. In addition, the use of transparent PDMS for device fabrication allows real-time monitoring of NP transport through each engineered barrier, as these processes are extremely difficult, if not impossible, to independently study *in vivo*. Moreover, quantitative tumor accumulation of NPs can be obtained by recovering spheroids for flow cytometry testing. Compared to conventional preclinical evaluation models, our TVOC model is easier to operate, cheaper, quicker, and more ethical without using animals.

DOI: 10.1021/acsnano.8b06846
ACS Nano 2018, 12, 11600−11609

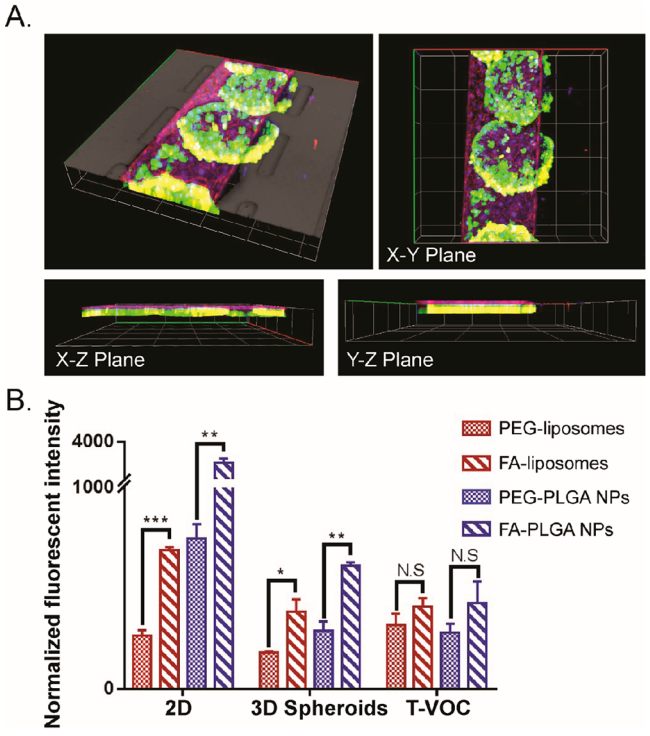

Figure 5. NP cellular uptake using 2D monolayers, 3D tumor spheroids, and the TVOC. (A) Confocal images showing the 3D structure and the *X*−*Y*, *X*−*Z*, and *Y*−*Z* planes of TVOC with 3D vasculature in the top channel and tumor spheroids at the bottom. HUVECs were stained for VE-cadherin (red) and nucleus (blue). Tumor spheroids were stained with a live−dead kit (green). Scale bars represent 200 μm. (B) Flow cytometry results of NP uptake by a 2D monolayer of SKOV3, 3D SKOV3 tumor spheroids in a 96-well plate, and tumor spheroids embedded in the TVOC model. Data show mean values and SD (n = 3). *, **, and * represent statistically significant difference $p < 0.05$, $p < 0.01$, and $p < 0.001$, respectively.**

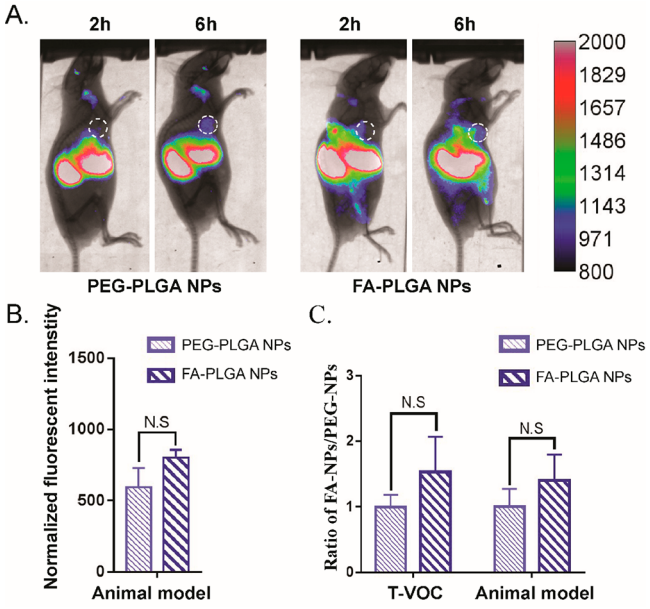

Figure 6. Targeting efficacies of PLGA NPs using *in vitro* and *in vivo* tumor models. (A) Whole animal images showing the biodistribution of PEG-PLGA NPs and FA-PLGA NPs after 2 and 6 h of NP injection. (B) Normalized fluorescent intensity of the *in vivo* tumor site after 6 h of NP injection. (C) Ratio of tumor accumulation of FA-PLGA NPs to PEG-PLGA NPs in the TVOC and animal model. Data show mean values and SD (n = 3).

Normal vasculature structure was established in the TVOC by culturing HUVECs under continuous medium perfusion. Intact HUVEC monolayers demonstrated tight intercellular junctions and, most importantly, the selective permeation of smaller dextran (20 kDa dextran) relative to large ones (70 kDa dextran), which is one of the primary functions of endothelium *in vivo*. The permeability coefficient of 70 kDa dextran is comparable to data reported *in vivo*.[36,37] The consequent TNF-α stimulation elevated vascular permeability and promoted extravasation of 70 kDa dextran, and the vascular permeability can be tuned by adjusting the stimulation time or concentrations of TNF-α.

The barrier functions of leaky vasculature and extracellular matrix were confirmed by investigating the extravasation and penetration of PEG-liposomes and PEG-PLGA NPs, two types of NPs with similar size and surface properties but different stiffness. Much slower transport of both NPs (radii ∼35 nm) was observed as opposed to dextran (Stokes' radii ∼3.3 nm for 20 kDa dextran and 6 nm for 70 kDa dextran). The presence of a TNF-α-treated endothelial monolayer hindered the extravasation of NPs, confirming the barrier property of the engineered leaky tumor vasculature. However, no significant differences were observed in the extravasation rates of PEG-liposomes and PEG-PLGA NPs, suggesting that NPs' stiffness might have little effect on NP extravasation, compared to other NP properties, such as size,[38] shape,[39−41] and surface charge.[42] This is in contrast to previous studies showing that the soft NPs were more deformable to pass through small pores compared to rigid NPs.[43,44]

In terms of NP tissue penetration, the TVOC model reveals that the gel matrix hinders the transport of NPs to a similar extent as the engineered endothelial barrier. However, no significant differences were observed in the TVOC regarding the tissue penetration of PEG-liposomes and PEG-PLGA NPs, probably because of the much smaller NP size (∼70 nm) than the pore sizes of Matrigel (∼500 nm).[45] In the M+H (Treated) model, NPs maintained a slow extravasation due to the limited porosity, while in the M+G model, NPs rapidly migrated across the membrane, but a majority of them accumulated in the peripheral area of the tumor tissue adjacent to the membrane due to the slow diffusion in the gel structure. In addition, the quick accumulation of migrated NPs adjacent to the membrane narrowed the difference of NPs' concentration across the porous membrane; hence NPs' transmembrane diffusion, primarily driven by a concentration gradient, gradually declined. Consequently, when both endothelial barrier and dense gel matrix were incorporated in the TVOC (M+G+H Treated), the permeability of NPs decreased significantly due to the combined effect of the two simulated barriers. By recreating the endothelial barrier and dense tumor ECM, the TVOC model provides a more physiological relevant *in vitro* tumor microenvironment for predicting the transport efficacy of nanoparticle-based drug delivery systems.

The NP tumor accumulation study demonstrates the capability of the TVOC in better mimicking the *in vivo* tumor microenvironment. 2D monolayer models show that the addition of FA-modification dramatically promotes NPs' cellular uptake due to active targeting, while the level of

DOI: 10.1021/acsnano.8b06846
ACS Nano 2018, 12, 11600−11609

enhancement became less significant in 3D tumor spheroid models and nonsignificant in the TVOC model and *in vivo* tumor models. As in 2D cell monolayer and 3D spheroids, NPs were statically cultured with cells, in which little hindrance existed in preventing the interaction between NPs and tumor cells. Such models provide straightforward cytotoxicity results, but they tend to overrate the effect of active targeting in drug delivery, while the passive targeting process is overlooked. Our TVOC model better mimics the key biological barriers involved in the transport of NPs *in vivo*, especially the key biological barriers involved in the passive targeting, which serves as a more reliable tumor model for nanoparticle-based drug screening.

CONCLUSIONS

This tumor-on-a-chip model recapitulates the key biological barriers in the tumor microenvironment, including the leaky tumor vasculature, tumor extracellular matrix, and 3D tumor structures. The TVOC model allows us to systematically investigate the effect of individual barrier as well as the combined effects on the NPs' extravasation and tumor accumulation. More importantly, the results obtained using the TVOC and animal models agree well, suggesting that the incorporation of a targeting ligand folic acid on NPs did not enhance tumor accumulation. By changing cell types or cytokines involved in the experimental setup, the TVOC model can serve as a versatile platform for drug evaluation in specifically customized tumor systems. Also, this model can be used to monitor the kinetics of NPs' tumor accumulation for hours up to days, thus allowing the prediction of NPs' long-term interactions with tumor tissue. In future studies, the TVOC model will be further validated using animal models for studying the effects of NPs' different properties such as size, shape, or targeting ligands on their tumor targeting, accumulation, and antitumor efficacy. The validated TVOC will enable a more in-depth understanding about how NPs take advantage of the EPR effect in tumor-selective drug delivery and will facilitate better prediction of the transport efficacy of NP formulations *in vitro* prior to expensive animal studies. These fundamental understanding will provide valuable insights into the rational design of better NPs for improved drug delivery.

METHODS

Design and Fabrication of the TVOC. The TVOC consists of two layers of microchannel with a porous membrane sandwiched between the layers. The top channel is 200 μm in width and 250 μm in height. The bottom channel has a 500 μm wide central spheroid-trapping region outlined by rectangular pillars (20 μm × 70 μm) and two 200 μm wide side channels to allow flow of excess fluid (Figure S1 in the Supporting Information). The microfluidic device was fabricated using standard photolithography and PDMS soft lithography techniques.[46] Briefly, the pattern was designed using the AutoCAD software and printed to a chrome mask as the template. Then, SU-8 photoresist was spin-coated on clean silicon wafers and baked, followed by UV exposure through the mask. After the postbaking procedure, the wafers were developed and washed to remove excess photoresist before use. To fabricate PDMS microfluidic devices, a mixture of silicon elastomer and curing agent (SYLGARD184, Dow Corning) was degassed and allowed to polymerize on an SU-8 patterned silicon mode at 80 °C for 1 h. The cross-linked PDMS slab was then peeled off from the wafer, cut into a single device, and tap cleaned. To fabricate the PDMS porous membrane, a chrome mask was patterned with an array of circles having a diameter of 10 μm and center-to-center spacing of 40 μm. AZ40XT photoresist was spin-coated on an HMDS-primed silicon wafer at a thickness of 5 μm to create the pattern, followed by deep reactive ion etching to further etch the silicon; then the top layer of AZ40XT was removed by reactive ion etching. The resulting silicon pillars were vertical with a height of 40 μm to ensure through pores of the PDMS membrane (thickness 10 μm). To fabricate the porous membrane, the wafer was silanized, spin-coated with PDMS at a speed of 6400 rpm, and prebaked at 80 °C for 1 min. Then, a clean PDMS slab with the top microchannel was placed on the patterned area of the wafer with a weight on top to ensure intimate contact between the PDMS slab and the wafer coated with PDMS. After 1 h of baking, the top PDMS slab together with the porous membrane was slowly peeled off from the wafer. To assemble the device, the PDMS layers were punched to create inlets and outlets. The oxygen plasma treated top channel was carefully aligned over the bottom channel. To prevent leakage, the double-layer device was placed in a 65 °C oven overnight to enhance bonding.

Cell Line and Cell Culture. Primary HUVECs and SKOV3 cells were purchased from the American Type Culture Collection. HUVECs were cultured in endothelial cell growth medium supplemented with EGM-2 SingleQuot kit supply and growth factors (EGM-2, Lonza, Switzerland). The HUVECs were used between passages 4 and 7. SKOV3 cells were cultured in high-glucose Dulbecco's modified Eagle medium (DMEM) supplemented with 10% fetal bovine serum, 100 U/mL penicillin, and 100 U/mL streptomycin (GIBCO, USA). All cells were cultured at 37 °C in a humidified 5% CO_2 atmosphere and trypsinized after reaching 70–80% confluence.

Establishing Leaky Tumor Vasculature in the TVOC Model. The vasculature compartment was established by culturing HUVECs in the top channel under medium perfusion. All the tubings, needles, and devices were sterilized under UV light for at least 1 h. Prior to cell seeding, the top microchannel was filled with 50 μg/mL fibronectin (Sigma-Aldrich, MO, USA) diluted in EGM-2 and incubated at 37 °C for 1 h to promote cell adhesion. The surface-treated microchannel was then filled with 10^8 cells/mL HUVECs suspended in EGM-2 and incubated statically for 4 h to allow cell attachment. The cell attachment was inspected under the microscope to confirm complete cell coverage of the microchannel. Then the device was connected to a programmable syringe pump (Harvard Apparatus, Holliston MA, USA) for continuous medium perfusion. HUVECs were found to generally reach confluence after a 2-day culture. Before the tests, the devices were checked using phase contract microscopy to ensure the formation of a complete HUVEC monolayer.

To mimic the leaky tumor vasculature, HUVECs was cultured in the device until confluence and treated with 20 ng/mL TNF-α (PeproTech, London, UK) statically. The effects of TNF-α on the confluent HUVEC monolayer were examined by immunostaining and a permeability test.

Immunostaining of HUVECs. To inspect the intercellular adherens junctions and cytoskeleton organization, HUVECs were imunostained for filamentous actin (F-actin), vascular endothelial cadherin (VE-cadherin), and nucleus. Hoechst 33342 and Alexa-Fluor647 Phalloidin were purchased from Invitrogen (Carlsbad, CA, USA). Paraformaldehyde, phosphate-buffered saline (PBS), bovine serum albumin (BSA), and Triton X-100 were obtained from Sigma-Aldrich (MO, USA). Cells were fixed with 4% paraformaldehyde, permeabilized with 0.1% Triton X for 10 min, and blocked with 2% BSA reconstituted in 1× PBS for 1 h at room temperature. After that, cells were incubated with either Alexa Fluor647 VE-cadherin mAb (SC-9989, Santa Cruz Biotechnology, USA) or Alexa Fluor647 Phalloidin for 1 h, followed by nucleus staining with Hoechst for 5 min. Fluorescence images were obtained using a confocal laser scanning microscope (CLSM, Zeiss 710, Jena, Germany).

Permeability of HUVEC Vasculature Structure. In order to characterize the effect of TNF-α on the integrity of the endothelial barrier, we quantified the permeability of engineered vasculature immediately after TNF-α stimulation by measuring the transport of 20 and 70 kDa FITC-dextran (Sigma-Aldrich, MO, USA) across the HUVEC monolayer. For comparison, the permeability of the empty

DOI: 10.1021/acsnano.8b06846
ACS Nano 2018, 12, 11600–11609

porous membrane was also examined. FITC-dextran was reconstituted in EGM-2 medium to a concentration of 0.05 mg/mL. Prior to the experiments, a standard curve of the correlation between dextran concentration and fluorescence intensity was obtained. To conduct the permeability test, the double-layer device was mounted on the stage of a CLSM, and the inlet of the top channel was connected to a programmable syringe pump. Dextran solution was introduced to the top channel at a flow rate of 0.3 μL/min. Once dextran was observed to completely fill the top channel, fluorescent images were acquired every 10 s for 30 min to observe the diffusion of dextran across the HUVEC monolayer toward the bottom channel.

The time lapse fluorescence images were analyzed by selecting a region of interest (ROI) at the background, top channel, and bottom channel (Figure S2 in the Supporting Information). The mean fluorescence intensity of the defined ROI and the fluorescence intensity profile over a certain distance in the selected region were extracted using Zen software (blue edition). The corresponding concentration of dextran in the bottom channel at each time point was calculated using the obtained standard curve.

As no additional pressure was applied to the microfluidic device, the transport of dextran was considered to be contributed by concentration gradient. Although the fluid flow in the top channel may cause transmembrane flux at the pore area, considering the slow laminar flow in the confined microchannel and the low porosity of the membrane (~5%), we assumed that dextran transport driven by convention was negligible; thus the transport of dextran across the endothelial monolayer was mainly attributed to diffusion. The permeability coefficient was calculated using eq 1:[47]

$$P = \frac{\Delta C_L V_L}{C_U A \Delta t} \quad (1)$$

where C_U is the initial concentration of the applied dextran in the upper channel, ΔC_L is the concentration change of dextran in the lower channel, V_L is the volume of the lower channel, A is the area of the membrane where tracers can transport between the upper and lower channels, and Δt is the assay time.

Preparation of Fluorescent Liposomes and PLGA Nanoparticles. Fluorescently labeled liposomes and PLGA nanoparticles were synthesized using the one-step microfluidic method as reported.[25,26] Briefly, the PDMS microfluidic device was designed with a flow-focusing region[48,49] and fabricated following the photolithography and softlithography process. To synthesize PEGylated liposomes (PEG-liposomes) and folic-acid-modified liposomes (FA-liposomes), lipid materials containing either 8 mol % PEG or 4 mol % PEG and 4 mol % FA were dissolved in chloroform, which was then removed by rotary evaporation. The remaining lipid film was redissolved in anhydrous isopropyl alcohol (IPA), and Dil dye was added to produce fluorescently labeled liposomes. The lipid-containing IPA was introduced to the central stream of the microfluidic device, while PBS was perfused into the second inlet at a volumetric flow rate ratio of 1:12.

To synthesize PEGylated PLGA nanoparticles (PEG-PLGA NPs) and folic-acid modified PLGA nanoparticles (FA-PLGA NPs), PEG-PLGA ligand was dissolved in acetonitrile, while FA-PEG-PLGA ligand was dissolved in a mixture of acetonitrile and dimethylformamide (DMF). Dil was added to have the same final concentration as that of liposomes. The polymer precursor was introduced into the central stream of the microfluidic device, while water was introduced into the second inlet. The flow rate ratio between polymer precursor and water was 4:10. All produced NPs were purified by dialysis using a cellulose membrane with a size of 10 kDa.

Characterization of Fluorescent NPs. *DLS Measurement.* The size and polydispersity index (PDI) of synthesized liposomes and PLGA NPs were measured using a Zetasizer Nano ZS (Malvern Instruments, Worcestershire, UK). Liposomes were diluted in PBS, and PLGA NPs were diluted in water to a concentration of 10% v/v.

TEM Observations. The synthesized liposomes and PLGA NPs were observed using a transmission electron microscope (Jeol, Tokyo, Japan) to further determine their sizes. Samples were dropped onto a copper TEM grid with a carbon film and air-dried at room temperature followed by negative staining using 1% uranyl acetate.

Transport of Fluorescent NPs in the TVOC. To investigate the extravasation and tumor accumulation of fluorescent NPs in the TVOC, three conditions were set up in the device to mimic the barrier functions of endothelium and rigid tumor stroma, including (a) TNF-α-treated HUVEC monolayers in the top channel and PBS-filled bottom channel (M+H Treated); (b) empty top channel and gel-filled bottom channel (M+G); and (c) TNF-α-treated HUVEC monolayers in the top channel and gel-filled bottom channel (M+G +H Treated). To mimic the tumor extracellular matrix, prechilled Matrigel was diluted to 20% (consistent with the following cellular uptake assay) and perfused into the bottom channel followed by polymerization. The device was mounted on the stage of a CLSM for real-time monitoring, and the permeability coefficients for fluorescent NPs were calculated using the method described above.

Quantitative Cellular Uptake Study Using Flow Cytometry. Cellular uptake of PEG-liposomes, FA-liposomes, PEG-PLGA NPs, and FA-PLGA NPs was studied on the 2D cell monolayer model, 3D tumor spheroids, and the TVOC model. For the 2D cellular uptake study, SKOV3 cells were seeded into a 24-well plate at a density of 2.5 $\times$ 10^5 cells/well and allowed to attach for 24 h. Then fluorescently labeled NPs were added into each well to a concentration of 10% v/v. Cells were incubated with NPs for 6 h. To prepare samples, cells were trypsinised, washed with PBS, and resuspended in 0.5 mL of PBS. Samples were measured with excitation and emission wavelengths at 549 and 565 nm, respectively, using a CytoFLEX flow cytometer (Beckman Coulter, CA, USA).

The 3D tumor spheroids were cultured using liquid overlay techniques. SKOV3 cells were seeded at a density of 5000 cells/well into a 96-well plate, which was precoated with 50 μL of 2% low-gelling-temperature agarose (Sigma-Aldrich, MO, USA). The spheroid formation was initiated by centrifugation (1000g, 10 min) of the plates. Cells were cultured for 7 days under conditions at 37 °C and 5% CO_2, and the formation of spheroids was observed under an optical microscope before the test. Spheroids were incubated with 10% Dil-labeled NPs for 6 h, then harvested from each well, washed with PBS, dissociated using Accumax solution (Sigma-Aldrich, MO, USA), and then resuspended in PBS to be analyzed.

To investigate the cellular uptake of spheroids in the TVOC model, spheroids were loaded into the bottom channel after confirming well-established leaky vasculature in the top channel. Prior to the test, Dil-labeled NPs were resuspended in DMEM to a concentration of 10% v/v. Intact tumor spheroids were harvested from the 96-well plate, and 10 spheroids were gathered into one Eppendorf tube. Collected spheroids were gently washed and resuspended in cold fresh medium, mixed with cold Matrigel (Corning, NY, USA) in a volume ratio of 4:1, and then pipetted into the bottom channel with 6−8 spheroids in one chip. To avoid gelation of Matrigel during the process, all pipet tips and tubes were prechilled at −20 °C overnight. Then the devices were incubated at 37 °C for 1 h to allow Matrigel polymerization, followed by 6 h perfusion of medium containing NPs in the top channel. At the end of the test, the devices were cooled in an ice bath to rethaw the Matrigel for 1 h. To ensure all the spheroids and detached single tumor cells were collected from the device, a tubing connected to an Eppendorf tube was inserted to the outlet, and PBS was perfused through the inlet to thoroughly flush the bottom channel until no remaining cellular structures could be observed. The collected spheroids were then washed with PBS, dissociated in Accumax solution, and then resuspended in PBS for flow cytometry analysis.

Biodistribution of Fluorescent NPs Using Animal Models. The *in vivo* targeting efficacy of PEG-PLGA NPs and FA-PLGA NPs was obtained using animal models. BALB/c nude mice (female, 8 weeks, ~16 g) were purchased from University of Queensland's Biological Resources (Brisbane, Australia) and maintained in a laminar flow room under constant temperature and humidity. All animal experiments were performed in accordance with protocols evaluated and approved by the ethics committee of the University of Queensland (Ethic Number: 2017000129). For animal experiments,

DOI: 10.1021/acsnano.8b06846
ACS Nano 2018, 12, 11600−11609

mice were subcutaneously (s.c.) injected with 0.1 mL of SKOV3 cell suspensions (10^7 cells/ml) in the right flank to establish the *in vivo* xenograft tumor model. The tumor-bearing mice were randomly divided into two groups with 8 mice in each group. Once the tumor size approached 0.5 cm in diameter, 0.1 mL of sterile saline containing either DiR-loaded PEG-PLGA NPs or FA-PLGA NPs was intravenously injected through the tail vein of mice at a dose of 120 μg DiR/mL. At time points of 2 and 6 h after the injection of NPs, mice were anaesthetised with isoflurane (2% in oxygen) and imaged using an *in vivo* MS FX Pro instrument (Bruker Corporation, MA, USA). The obtained images were analyzed using imageJ to determine the localization of fluorescent NPs.

Statistical Analysis. Statistical analysis of the data was performed with an unpaired Student's *t* test using Microsoft Excel for Windows 2011, and *p* values of <0.05, <0.01, and <0.001 were marked as *, **, and ***, respectively.

Data Availability. All relevant data are available from the authors upon reasonable request.

ASSOCIATED CONTENT

Supporting Information

The Supporting Information is available free of charge on the ACS Publications website at DOI: 10.1021/acsnano.8b06846.

Images of the fabricated microfluidic device, illustration of the analysis of the fluorescence images, schematic illustration of the device for synthesizing nanoparticles, and TEM images of the prepared nanoparticles (PDF)

AUTHOR INFORMATION

Corresponding Author

*E-mail: z.chunxia@uq.edu.au.

ORCID

Hao-Fei Wang: 0000-0001-8906-1798
Bijun Zeng: 0000-0002-6199-0584
Dong Chen: 0000-0002-8904-9307
David A. Weitz: 0000-0001-6678-5208
Chun-Xia Zhao: 0000-0002-3365-3759

Author Contributions

C.-X.Z. devised the project, designed the study, and supervised the project. H.-F.W. carried out the experiment and wrote the manuscript. R.R., Y.H., and Y.L. helped with the animal experiment. B.-J.Z. provided suggestions on cell culture and animal experiments. D.C. and D.W. contributed to the final version of the manuscript.

Notes

The authors declare no competing financial interest.

ACKNOWLEDGMENTS

This research was supported by the Australian Research Council under Future Fellowship project FT140100726. This work was performed in part at the Queensland node of the Australian National Fabrication Facility (ANFF). We acknowledge the scientists and technicians of ANFF in microfluidic device fabrication and *in vitro* confocal imaging. We thank the Australian Microscopy & Microanalysis Research Facility at the Centre for Microscopy and Microanalysis, The University of Queensland, for providing the TEM for imaging. The work at Harvard was supported by the NSF (DMR-1708729), the Harvard MRSEC (DMR-1420570), and the NIH (R01EB014703).

REFERENCES

(1) Maeda, H.; Nakamura, H.; Fang, J. The Epr Effect for Macromolecular Drug Delivery to Solid Tumors: Improvement of Tumor Uptake, Lowering of Systemic Toxicity, and Distinct Tumor Imaging *in vivo*. *Adv. Drug Delivery Rev.* **2013**, *65*, 71−79.

(2) Torchilin, V. Tumor Delivery of Macromolecular Drugs Based on the EPR Effect. *Adv. Drug Delivery Rev.* **2011**, *63*, 131−135.

(3) Iyer, A. K.; Khaled, G.; Fang, J.; Maeda, H. Exploiting the Enhanced Permeability and Retention Effect for Tumor Targeting. *Drug Discovery Today* **2006**, *11*, 812−818.

(4) Singh, R.; Lillard, J. W., Jr Nanoparticle-Based Targeted Drug Delivery. *Exp. Mol. Pathol.* **2009**, *86*, 215−223.

(5) Sun, Q.; Tan, S. H.; Chen, Q.; Ran, R.; Hui, Y.; Chen, D.; Zhao, C.-X., Microfluidic Formation of Coculture Tumor Spheroids with Stromal Cells as a Novel 3D Tumor Model for Drug Testing. *ACS Biomater. Sci. Eng.* **2018**, DOI: 10.1021/acsbiomaterials.8b00904

(6) Toley, B. J.; Tropeano Lovatt, Z. G.; Harrington, J. L.; Forbes, N. S. Microfluidic Technique to Measure Intratumoral Transport and Calculate Drug Efficacy Shows That Binding Is Essential for Doxorubicin and Release Hampers Doxil. *Integr Biol.* **2013**, *5*, 1184−96.

(7) Albanese, A.; Lam, A. K.; Sykes, E. A.; Rocheleau, J. V.; Chan, W. C. W. Tumour-on-a-Chip Provides an Optical Window into Nanoparticle Tissue Transport. *Nat. Commun.* **2013**, *4*, 2718.

(8) Ruppen, J.; Cortes-Dericks, L.; Marconi, E.; Karoubi, G.; Schmid, R. A.; Peng, R.; Marti, T. M.; Guenat, O. T. A Microfluidic Platform for Chemoresistive Testing of Multicellular Pleural Cancer Spheroids. *Lab Chip* **2014**, *14*, 1198−205.

(9) Kim, Y.; Lobatto, M. E.; Kawahara, T.; Chung, B. L.; Mieszawska, A. J.; Sanchez-Gaytan, B. L.; Fay, F.; Senders, M. L.; Calcagno, C.; Becraft, J. Probing Nanoparticle Translocation across the Permeable Endothelium in Experimental Atherosclerosis. *Proc. Natl. Acad. Sci. U. S. A.* **2014**, *111*, 1078−1083.

(10) Ho, Y. T.; Adriani, G.; Beyer, S.; Nhan, P.-T.; Kamm, R. D.; Kah, J. C. Y. A Facile Method to Probe the Vascular Permeability of Nanoparticles in Nanomedicine Applications. *Sci. Rep.* **2017**, *7*, 707.

(11) Tang, Y.; Soroush, F.; Sheffield, J. B.; Wang, B.; Prabhakarpandian, B.; Kiani, M. F. A Biomimetic Microfluidic Tumor Microenvironment Platform Mimicking the Epr Effect for Rapid Screening of Drug Delivery Systems. *Sci. Rep.* **2017**, *7*, 9359.

(12) Kwak, B.; Ozcelikkale, A.; Shin, C. S.; Park, K.; Han, B. Simulation of Complex Transport of Nanoparticles around a Tumor Using Tumor-Microenvironment-on-Chip. *J. Controlled Release* **2014**, *194*, 157−167.

(13) Fox, S. I. *Human Physiology*, 9th ed.; McGraw-Hill Press: New York, USA, 2006; pp 501−502.

(14) Madge, L. A.; Pober, J. S. TNF Signaling in Vascular Endothelial Cells. *Exp. Mol. Pathol.* **2001**, *70*, 317−325.

(15) Kakei, Y.; Akashi, M.; Shigeta, T.; Hasegawa, T.; Komori, T. Alteration of Cell−Cell Junctions in Cultured Human Lymphatic Endothelial Cells with Inflammatory Cytokine Stimulation. *Lymphatic Res. Biol.* **2014**, *12*, 136−143.

(16) Martin, T. A.; Mason, M. D.; Jiang, W. G. Tight Junctions in Cancer Metastasis. *Front. Biosci., Landmark Ed.* **2011**, *16*, 898−936.

(17) Hashizume, H.; Baluk, P.; Morikawa, S.; McLean, J. W.; Thurston, G.; Roberge, S.; Jain, R. K.; McDonald, D. M. Openings between Defective Endothelial Cells Explain Tumor Vessel Leakiness. *Am. J. Pathol.* **2000**, *156*, 1363−1380.

(18) Sarin, H.; Kanevsky, A. S.; Wu, H.; Sousa, A. A.; Wilson, C. M.; Aronova, M. A.; Griffiths, G. L.; Leapman, R. D.; Vo, H. Q. Physiologic Upper Limit of Pore Size in the Blood-Tumor Barrier of Malignant Solid Tumors. *J. Transl. Med.* **2009**, *7*, 51.

(19) Yuan, S. Y.; Rigor, R. R. In *Regulation of Endothelial Barrier Function*; Colloquium Series on Integrated Systems Physiology: From Molecule to Function; Morgan & Claypool Life Sciences, 2011; pp 1−146.

(20) Allen, T. M.; Cullis, P. R. Liposomal Drug Delivery Systems: From Concept to Clinical Applications. *Adv. Drug Delivery Rev.* **2013**, *65*, 36−48.

(21) Acharya, S.; Sahoo, S. K. Plga Nanoparticles Containing Various Anticancer Agents and Tumour Delivery by Epr Effect. *Adv. Drug Delivery Rev.* **2011**, *63*, 170−183.
(22) Davis, M. E.; Shin, D. M. Nanoparticle Therapeutics: An Emerging Treatment Modality for Cancer. *Nat. Rev. Drug Discovery* **2008**, *7*, 771.
(23) Liu, Y.; Hui, Y.; Ran, R.; Yang, G. Z.; Wibowo, D.; Wang, H. F.; Middelberg, A. P. J.; Zhao, C. X. Synergetic Combinations of Dual-Targeting Ligands for Enhanced *in vitro* and *in vivo* Tumor Targeting. *Adv. Healthcare Mater.* **2018**, *7*, No. e1800106.
(24) Ran, R.; Wang, H.; Liu, Y.; Hui, Y.; Sun, Q.; Seth, A.; Wibowo, D.; Chen, D.; Zhao, C. X. Microfluidic Self-Assembly of a Combinatorial Library of Single- and Dual-Ligand Liposomes for *in vitro* and *in vivo* Tumor Targeting. *Eur. J. Pharm. Biopharm.* **2018**, *130*, 1−10.
(25) Ran, R.; Middelberg, A. P.; Zhao, C.-X. Microfluidic Synthesis of Multifunctional Liposomes for Tumour Targeting. *Colloids Surf., B* **2016**, *148*, 402−410.
(26) Baby, T.; Liu, Y.; Middelberg, A. P. J.; Zhao, C.-X. Fundamental Studies on Throughput Capacities of Hydrodynamic Flow-Focusing Microfluidics for Producing Monodisperse Polymer Nanoparticles. *Chem. Eng. Sci.* **2017**, *169*, 128−139.
(27) Netti, P. A.; Berk, D. A.; Swartz, M. A.; Grodzinsky, A. J.; Jain, R. K. Role of Extracellular Matrix Assembly in Interstitial Transport in Solid Tumors. *Cancer Res.* **2000**, *60*, 2497−503.
(28) Jain, R. K.; Stylianopoulos, T. Delivering Nanomedicine to Solid Tumors. *Nat. Rev. Clin. Oncol.* **2010**, *7*, 653.
(29) Chen, T.; Li, C.; Li, Y.; Yi, X.; Wang, R.; Lee, S. M.-Y.; Zheng, Y. Small-Sized Mpeg−Plga Nanoparticles of Schisantherin a with Sustained Release for Enhanced Brain Uptake and Anti-Parkinsonian Activity. *ACS Appl. Mater. Interfaces* **2017**, *9*, 9516−9527.
(30) Yuan, F.; Leunig, M.; Huang, S. K.; Berk, D. A.; Papahadjopoulos, D.; Jain, R. K. Mirovascular Permeability and Interstitial Penetration of Sterically Stabilized (Stealth) Liposomes in a Human Tumor Xenograft. *Cancer Res.* **1994**, *54*, 3352−3356.
(31) Wu, N. Z.; Da, D.; Rudoll, T. L.; Needham, D.; Whorton, A. R.; Dewhirst, M. W. Increased Microvascular Permeability Contributes to Preferential Accumulation of Stealth Liposomes in Tumor Tissue. *Cancer Res.* **1993**, *53*, 3765−70.
(32) Rygh, C. B.; Qin, S.; Seo, J. W.; Mahakian, L. M.; Zhang, H.; Adamson, R.; Chen, J. Q.; Borowsky, A. D.; Cardiff, R. D.; Reed, R. K. Longitudinal Investigation of Permeability and Distribution of Macromolecules in Mouse Malignant Transformation Using Pet. *Clin. Cancer Res.* **2011**, *17*, 550−559.
(33) Zhang, L.; Feng, Q.; Wang, J.; Zhang, S.; Ding, B.; Wei, Y.; Dong, M. D.; Ryu, J.; Yoon, T.; Shi, X.; Sun, J.; Jiang, X. Microfluidic Synthesis of Hybrid Nanoparticles with Controlled Lipid Layers: Understanding Flexibility-Regulated Cell-Nanoparticle Interaction. *ACS Nano* **2015**, *9*, 9912−9921.
(34) Anselmo, A. C.; Zhang, M.; Kumar, S.; Vogus, D. R.; Menegatti, S.; Helgeson, M. E.; Mitragotri, S. Elasticity of Nanoparticles Influences Their Blood Circulation, Phagocytosis, Endocytosis, and Targeting. *ACS Nano* **2015**, *9*, 3169−3177.
(35) Hui, Y.; Wibowo, D.; Liu, Y.; Ran, R.; Wang, H.-F.; Seth, A.; Middelberg, A. P.; Zhao, C.-X. Understanding the Effects of Nanocapsular Mechanical Property on Passive and Active Tumor Targeting. *ACS Nano* **2018**, *12*, 2846−2857.
(36) Dreher, M. R.; Liu, W.; Michelich, C. R.; Dewhirst, M. W.; Yuan, F.; Chilkoti, A. Tumor Vascular Permeability, Accumulation, and Penetration of Macromolecular Drug Carriers. *J. Natl. Cancer Inst.* **2006**, *98*, 335−44.
(37) Yuan, F.; Chen, Y.; Dellian, M.; Safabakhsh, N.; Ferrara, N.; Jain, R. K. Time-Dependent Vascular Regression and Permeability Changes in Established Human Tumor Xenografts Induced by an Anti-Vascular Endothelial Growth Factor/Vascular Permeability Factor Antibody. *Proc. Natl. Acad. Sci. U. S. A.* **1996**, *93*, 14765−14770.
(38) Pegaz, B.; Debefve, E.; Ballini, J. P.; Konan-Kouakou, Y. N.; van den Bergh, H. Effect of Nanoparticle Size on the Extravasation and the Photothrombic Activity of Meso(P-Tetracarboxyphenyl)-Porphyrin. *J. Photochem. Photobiol., B* **2006**, *85*, 216−22.
(39) Uhl, C.; Gao, Y.; Zhou, S.; Liu, Y. The Shape Effect on Polymer Nanoparticle Transport in a Blood Vessel. *RSC Adv.* **2018**, *8*, 8089−8100.
(40) Decuzzi, P.; Pasqualini, R.; Arap, W.; Ferrari, M. Intravascular Delivery of Particulate Systems: Does Geometry Really Matter? *Pharm. Res.* **2009**, *26*, 235−43.
(41) Gentile, F.; Chiappini, C.; Fine, D.; Bhavane, R. C.; Peluccio, M. S.; Cheng, M. M.; Liu, X.; Ferrari, M.; Decuzzi, P. The Effect of Shape on the Margination Dynamics of Non-Neutrally Buoyant Particles in Two-Dimensional Shear Flows. *J. Biomech.* **2008**, *41*, 2312−8.
(42) Thurston, G.; McLean, J. W.; Rizen, M.; Baluk, P.; Haskell, A.; Murphy, T. J.; Hanahan, D.; McDonald, D. M. Cationic Liposomes Target Angiogenic Endothelial Cells in Tumors and Chronic Inflammation in Mice. *J. Clin. Invest.* **1998**, *101*, 1401−13.
(43) Kersey, F. R.; Merkel, T. J.; Perry, J. L.; Napier, M. E.; DeSimone, J. M. Effect of Aspect Ratio and Deformability on Nanoparticle Extravasation through Nanopores. *Langmuir* **2012**, *28*, 8773−8781.
(44) Parodi, A.; Quattrocchi, N.; van de Ven, A. L.; Chiappini, C.; Evangelopoulos, M.; Martinez, J. O.; Brown, B. S.; Khaled, S. Z.; Yazdi, I. K.; Enzo, M. V.; Isenhart, L.; Mauro, F.; Tasciotti, E. Synthetic Nanoparticles Functionalized with Biomimetic Leukocyte Membranes Possess Cell-Like Functions. *Nat. Nanotechnol.* **2013**, *8*, 61−8.
(45) Lam, N. T.; Lam, H.; Sturdivant, N. M.; Balachandran, K. Fabrication of a Matrigel-Collagen Semi-Interpenetrating Scaffold for Use in Dynamic Valve Interstitial Cell Culture. *Biomed. Mater.* **2017**, *12*, 045013.
(46) Anderson, J. R.; Chiu, D. T.; Wu, H.; Schueller, O.; Whitesides, G. M. Fabrication of Microfluidic Systems in Poly (Dimethylsiloxane). *Electrophoresis* **2000**, *21*, 27−40.
(47) Yuan, W.; Li, G.; Fu, B. M. Effect of Surface Charge of Immortalized Mouse Cerebral Endothelial Cell Monolayer on Transport of Charged Solutes. *Ann. Biomed. Eng.* **2010**, *38*, 1463−1472.
(48) Ran, R.; Sun, Q.; Baby, T.; Wibowo, D.; Middelberg, A. P. J.; Zhao, C.-X. Multiphase Microfluidic Synthesis of Micro- and Nanostructures for Pharmaceutical Applications. *Chem. Eng. Sci.* **2017**, *169*, 78−96.
(49) Zhao, C.-X. Multiphase Flow Microfluidics for the Production of Single or Multiple Emulsions for Drug Delivery. *Adv. Drug Delivery Rev.* **2013**, *65*, 1420−1446.

DOI: 10.1021/acsnano.8b06846
ACS Nano 2018, 12, 11600−11609